

Molecular imaging by optically-detected electron spin resonance of nitrogen- vacancies in nanodiamond

Alex Hegyi* and Eli Yablonovitch

Department of Electrical Engineering and Computer Sciences

University of California, Berkeley

*Email: hegyi@eecs.berkeley.edu

TITLE: Molecular imaging by optically-detected electron spin resonance of nitrogen-vacancies in nanodiamond

INTRO PARAGRAPH: Molecular imaging refers to a class of noninvasive biomedical imaging techniques with the sensitivity and specificity to image biochemical variations *in-vivo*¹. An ideal molecular imaging technique visualizes a biochemical target according to a range of criteria, including high spatial and temporal resolution, high contrast relative to non-targeted tissues, depth-independent penetration into tissue, lack of harm to the organism under study, and low cost. Because no existing molecular imaging modality is ideal for all purposes, new imaging approaches are needed. Here we demonstrate a novel molecular imaging approach, called nanodiamond imaging, that uses nanodiamonds containing nitrogen-vacancy (NV) color centers²⁻⁴ as an imaging agent, and image nanodiamond targets in pieces of chicken breast. Nanodiamonds can be tagged with biologically active molecules so they bind to specific receptors⁵⁻⁸; their distribution can then be quantified *in-vivo* via optically-detected magnetic resonance of the NVs. In effect, we are demonstrating Optically-Detected Functional-Electron-Spin-Resonance-Imaging, OD-f-ESRI. By combining optical detection with magnetic resonance, nanodiamond imaging achieves high sensitivity and high spatial resolution. It is absent of the complications of ionizing radiation, and the cost should be similar to all-optical imaging. Because nanodiamond imaging is limited by the depth of optical penetration into tissue⁹ to depths of a few cm, nanodiamond imaging should open up new avenues of investigation for applications where high depth penetration is not required, such as in small-animal imaging^{10,11}, tumor margin imaging¹², sentinel lymph node mapping^{8,13}, and perhaps mammography.

TEXT:

For the purposes of this paper, existing biomedical imaging techniques can be broken down according to two different classes: *anatomical* techniques, such as magnetic resonance imaging, x-ray/x-ray computed tomography (CT), and ultrasound, and *molecular* techniques, such as positron emission tomography (PET), single-photon emission computed tomography (SPECT), and fluorescence optical imaging. The chief difference between anatomical and molecular techniques is anatomical techniques have higher spatial resolution than molecular techniques, while molecular techniques have much higher sensitivity and specificity to image subtle biochemical variations within an organism, though at significantly lower spatial resolutions. (For a good comparison of existing imaging techniques, consult Table 1 of Ref. [1].) Many molecular imaging techniques make use of an imaging agent, which is the combination of a biological molecule that interacts with a particular target and a marker that is sensed by an imaging system. Nanodiamond imaging operates in this way, and it exploits a serendipitous combination of many physical properties of its NV-nanodiamond imaging agent that give it the best aspects of both imaging classes: the high specificity and sensitivity of molecular imaging, yet at the high spatial resolutions achievable with anatomical imaging.

The first set of useful physical properties come from the nanodiamond host. Nanodiamonds are an ideal nanoparticle for imaging because of their low cost, scalable fabrication methods, non-toxicity, and the facility with which their surfaces can be modified to attach to various biomolecules^{5-8,14}, providing a robust method of generating

biological specificity. The inclusion of NVs, which are a type of point defect, in the nanodiamonds transforms them into sensitive optical and magnetic probes.

By themselves, the optical properties of the NV are amenable to biological imaging. The fluorescence spectrum of the NV extends from ~630 nm to ~800 nm, peaking around 700 nm, and roughly matching the near-infrared window in biological tissue⁹. The fluorescence has a high quantum yield, it is stable (i.e., doesn't bleach or blink), and occurs at a timescale ($\tau \approx 17$ ns, in nanodiamond¹⁵) significantly longer than biological autofluorescence lifetimes such that time-gating enhances the signal-to-noise ratio¹⁶. These characteristics have created interest in using NV-containing nanodiamonds as fluorescent probes for biology^{15,17}, as a replacement for toxic quantum dots and bleachable organic dyes.

The high magnetic sensitivity of the NV also comes from the diamond host. The NV's energy levels exist in the diamond bandgap, so the NV acts like an isolated atom. Its unpaired electrons give rise to a triplet ground state, and because this state is weakly coupled to the diamond lattice, it has long spin relaxation (T_1) and spin coherence (T_2) lifetimes, or narrow electron spin resonance (ESR) linewidths, even at room temperature (typical values for NV in nanodiamond might be $T_1 = 1$ ms and $T_2 = 1$ μ s [18]). However, the significance of the NV is due to the interaction of its optical and magnetic properties: the spin state can be polarized and detected optically, even for a single NV at room temperature (notably, these features make the NV a prime qubit candidate for quantum computation^{19,20}).

The narrow ESR linewidths provide high spatial resolution in a magnetic gradient, while the optical detection provides high measurement sensitivity; many have recognized the significance of this combination for biological applications. NV-based optically detected ESR has high enough spatial resolution and sensitivity that nanodiamond magnetometers^{21,22} based on this principle have been proposed as detectors to perform nanoscale magnetic resonance imaging of biological molecules. Also, in combination with the stable fluorescence, the spin properties of the NV allow high resolution localization and tracking of NV-nanodiamonds in live cells^{23,24}.

However, what we propose, imaging the nanodiamond concentration within the scattering tissue of macroscopic organisms, differs significantly from existing work. The existing work has relied on microscopic fields of view to get high optical intensity in a focused laser spot and clear optical access to the NVs, and high intensity microwaves for coherent microwave pulses (i.e., Rabi nutation rate greater than the decoherence rate). Because we aim to illuminate a substantial fraction of an organism, we use much lower (by up to five orders of magnitude) optical intensity, and in addition use incoherent microwave excitation (i.e., at much lower excitation powers). To our knowledge, this is the first report of combining optical detection with magnetic resonance for imaging within scattering tissue, though a similar technique utilizing a non-resonant magnetic field effect, magnetofluorescence imaging²⁵, has been proposed.

As an overview of our particular version of optically-detected ESR, we make use of a magnetic field-free point, where only those NVs near the field-free point are resonant with a microwave field at 2.869 GHz. Optical excitation polarizes the NV spins into a

highly fluorescent state, and the microwaves mix only those spins near the field-free point into a less fluorescent state. Thus, the microwaves decrease the fluorescence by an amount proportional to the nanodiamond concentration at the field-free point. By sweeping the field-free point across an organism and tracking the changes in fluorescence, a quantitative map of the nanodiamond concentration as a function of position can be obtained.

Critical to the functioning of nanodiamond imaging are the NV's properties of optically-induced spin polarization and optical spin detection. As shown in Fig. 1a and Fig. 1b, the electronic ground state of the NV is a spin triplet, with a zero-magnetic-field splitting of 2.869 GHz between the $m_s = 0$ and the $m_s = \pm 1$ sublevels. The NV spin is pumped into the $m_s = 0$ sublevel upon optical excitation, because the intermediate singlet states decay preferentially to the $m_s = 0$ sublevel. Furthermore, because the $m_s = \pm 1$ can decay non-radiatively while the $m_s = 0$ decays only radiatively, $m_s = \pm 1$ fluoresces more dimly than $m_s = 0$. Microwaves resonant with the spin transitions mix the spin sublevels, and by placing a magnetic field along the NV axis (Fig. 1c), the ± 1 spin sublevels split relative to each other at a rate of 56 GHz T⁻¹ (approximately equivalent to the Zeeman splitting of a free electron). In nanodiamond powder, transitions at all frequencies between the two extreme frequencies occur because of the random orientation of individual nanodiamonds with respect to the magnetic field.

After optical pumping of the NV spins into the bright $m_s = 0$ sublevel, microwaves at 2.869 GHz mix the spin sublevels, leading to an observable decrease in fluorescence, but only in the *absence* of a magnetic field (Fig. 1d), i.e. at the field-free point. Thus, the concentration of nanodiamonds at the field-free point can be inferred by the decrease in intensity of the NV fluorescence. As the field-free point is scanned in one dimension across a point of nanodiamonds (Fig. 1e), we obtain the point-spread function (PSF) for our imaging system (Fig. 1f); Supplementary Information 3 describes in detail how we obtained this.

To image a 2D slice or a 3D volume of the nanodiamond concentration within an organism, we can scan the field-free point across it in two or three dimensions. Two-dimensional projections of the nanodiamond concentration can be obtained with a field-free line; projections from different angles can be combined into a 3D image using a standard reconstruction algorithm, as in computed tomography. Forming a 3D image in this way will generally lead to higher SNR in the same measurement time than 3D scanning of a field-free point, because the measurement is multiplexed (i.e., information pertinent to many voxels is sampled at once).

The use of a field-free point or line, as inspired by *x*-space magnetic particle imaging²⁶, distinguishes this kind of spin resonance imaging from traditional MRI. MRI relies on the coherent precession of spins, within a magnetic gradient, across the sample volume. In nanodiamond imaging, the 2.869 GHz zero-field splitting of the triplet levels acts as an effective magnetic field directed along the diamond's [111] crystalline axis, yet the orientation of this effective magnetic field relative to any applied gradient is arbitrary, and it creates an uncertainty in the precession frequency of the various NV spins. However, the advantage of working at the field-free point is the resonance frequency only depends on the crystal field, which is independent of the nanodiamond orientation. The

gradient that surrounds the field-free point smears out the resonance, but that is acceptable because it does so predictably.

A detailed description of the imaging system (Fig. 2) can be found in Supplementary Information 1. Briefly, a red LED attached to a current source provides stable optical excitation at 610 nm to 630 nm and generates $\sim 1 \text{ W cm}^{-2}$ of red light at the sample. Fluorescence is detected by a single photodiode; note that positional information about the nanodiamonds is completely encoded into the fluorescence intensity and not spatially resolved at the detector, although using a multi-element detector may provide additional information for image reconstruction. Four permanent magnets in a cylindrical quadrupolar arrangement create a field-free line at the center of a 1 T m^{-1} gradient, for 2D projection imaging along the z -axis. The line can be shifted relative to the sample via a dipolar arrangement of electromagnets in the x - and y - axes to form images with a 1 cm^2 field of view. The microwaves are modulated at 379 Hz, and the corresponding change in fluorescence is synchronously detected.

Many images of nanodiamond phantoms inside $1 \text{ cm} \times 1 \text{ cm} \times 2 \text{ cm}$ pieces of chicken breast were taken to demonstrate the imaging technique. All phantoms were made out of double-sticky tape covered with a $\sim 4 \mu\text{g mm}^{-2}$ areal density of nanodiamonds, as discussed in Supplementary Information 2. Shown in Fig. 3 are photographs of the phantoms (a), a diagram and photograph of the chicken breast during the experiment (b), the raw images and deconvolved images of the phantom outside of chicken breast obtained from the imaging system (c), raw and deconvolved images of the phantom under 5 mm of chicken (d; also the situation depicted in b), and for the 'L' phantom under 12 mm of chicken (e). Note no change in resolving power with depth, as expected. Also, once inside the chicken breast, a human observer can no longer see the phantoms, so there is some rotation of the phantom relative to the images of the phantoms outside of the chicken. The PSF in Fig. 3f is obtained from revolving the PSF in Fig. 1f.

The resolution of this particular imaging system depends on the width of the PSF, which varies with the strength of the magnetic field gradient. With a 1 T m^{-1} gradient, the central peak of the PSF (indicated on Fig. 1f) has a FWHM of roughly $800 \mu\text{m}$. The amplitude of the PSF scales roughly as r^{-1} , where r is the distance from the field-free point to a test point of nanodiamonds, because the fraction of nanodiamonds still resonant with the microwaves also scales as this factor (gradient in Fig. 1c). Deviations from this scaling primarily come from strain in the nanodiamonds causing inhomogeneous broadening of the zero-field transition (reducing the maximum modulation of the fluorescence achievable with a single microwave frequency), the development of an anti-crossing between the $m_s = 1$ and $m_s = -1$ states with applied magnetic field (causing a pronounced first dip) and a lowering in energy of the $m_s = 0$ state at higher magnetic fields (blue-shifting the anti-crossing above the microwave frequency and increasing the proportion of NV transitions resonant with the microwaves).

The sensitivity to detect the presence of nanodiamonds at the surface of a tissue sample is measured as $2.2 \text{ mM mm}^3 \text{ Hz}^{-1/2}$, i.e., a 2.2 millimolar concentration of carbon atoms in a mm^3 voxel can be detected with a SNR of unity in one Hz of measurement bandwidth, as explained in Supplementary Information 4. There are many performance enhancements we can expect which would drive sensitivity much higher, more than 7 orders of

magnitude in combination. Most notably, different NV-nanodiamond synthesis techniques may increase the ratio of NVs to carbon atoms: sintering of detonation nanodiamond may increase this ratio to 1 percent¹⁸, whereas the nanodiamonds used in the current experiment contain 6 ppm NV, introduced by ion implantation and annealing. Further sensitivity enhancements, discussed in detail in Supplementary Information 4, are expected from pulsing the optical and/or microwave excitation, enhancing the amount of fluorescence collected, time-gating the fluorescence collection, water-cooling the organism to allow higher optical excitation intensity, and reducing nanodiamond strain (which would also produce higher resolution).

For a reference point, it is helpful to make a comparison to existing imaging techniques. In Figure 4, we attempt to compare nanodiamond imaging (NDI) to several popular imaging techniques on the basis of sensitivity (in terms of minimum detectable mass of imaging agent), resolution, and cost. The data for existing techniques were obtained from four references, and details of how the graph was prepared are in Supplementary Information 5. For existing techniques, there is a clear breakdown into two groups: those with higher resolution but lower sensitivity (labeled “Anatomical”), and those with higher sensitivity but lower resolution (labeled “Molecular”). The current implementation of NDI (a) has higher mass sensitivity than existing anatomical techniques and higher resolution than the molecular techniques. With four orders of magnitude sensitivity improvement (around 0.03% of the identified avenues for improvement), and less than one order of magnitude improvement in resolution—possible by increasing the magnetic field gradient or reducing nanodiamond strain—nanodiamond imaging would rival both molecular imaging in terms of sensitivity and anatomical imaging in terms of resolution. There are also no obvious barriers to low cost; the system is not significantly more complex than an optical imaging system.

The main drawback is the limited depth penetration due to the attenuation of light within tissue. The optical excitation must pass through tissue to excite the NVs and generate fluorescence; furthermore, the NV spin polarization, and hence the modulation of the fluorescence achievable with the microwaves, is proportional to the optical excitation; finally, the fluorescence also has to escape from the tissue. Combined, these factors imply a steep drop-off of signal with depth. However, the potential for preclinical imaging is high, and nanodiamond imaging may be useful for certain kinds of depth-limited clinical imaging: chicken breast may be a good surrogate for human breast tissue due to its similar optical properties²⁷, and since we have already demonstrated imaging at a depth of over 1 cm in chicken breast, with improvements it may be possible to image at depths of 2-3 cm or more.

REFERENCES:

1. James, M. L. & Gambhir, S. S. A molecular imaging primer: modalities, imaging agents, and applications. *Physiological reviews* **92**, 897–965 (2012).
2. Budker, D. Diamond nanosensors: The sense of colour centres. *Nature Physics* **7**, 453–454 (2011).
3. Awschalom, D. D., Epstein, R. & Hanson, R. The diamond age of spintronics. *Scientific American* **297**, 84–91 (2007).
4. Aharonovich, I., Greentree, A. D. & Prawer, S. Diamond photonics. *Nature Photonics* **5**, 397–405 (2011).
5. Zhang, X.-Q. *et al.* Multimodal nanodiamond drug delivery carriers for selective targeting, imaging, and enhanced chemotherapeutic efficacy. *Advanced materials (Deerfield Beach, Fla.)* **23**, 4770–5 (2011).
6. Schrand, A., Hens, S. A. C. & Shenderova, O. Nanodiamond Particles: Properties and Perspectives for Bioapplications. *Critical Reviews in Solid State and Materials Sciences* **34**, 18–74 (2009).
7. Chao, J.-I. *et al.* Nanometer-sized diamond particle as a probe for biolabeling. *Biophysical journal* **93**, 2199–208 (2007).
8. Vijayanthimala, V. *et al.* The long-term stability and biocompatibility of fluorescent nanodiamond as an in vivo contrast agent. *Biomaterials* **33**, 7802–7794 (2012).
9. Tuchin, V. *Tissue Optics: Light Scattering Methods and Instruments for Medical Diagnosis*. 9 (SPIE Publications: 2000).at <<http://www.amazon.com/Tissue-Optics-Scattering-Instruments-Diagnosis/dp/0819464333>>
10. de Kemp, R. A., Epstein, F. H., Catana, C., Tsui, B. M. W. & Ritman, E. L. Small-animal molecular imaging methods. *Journal of nuclear medicine : official publication, Society of Nuclear Medicine* **51 Suppl 1**, 18S–32S (2010).
11. Meikle, S. R., Kench, P., Kassiou, M. & Banati, R. B. Small animal SPECT and its place in the matrix of molecular imaging technologies. *Physics in medicine and biology* **50**, R45–61 (2005).
12. Patlak, M. Nanoimaging devices illuminate tumor margins during surgery. *Journal of the National Cancer Institute* **103**, 173–4 (2011).
13. Bonnema, J. & van de Velde, C. J. H. Sentinel lymph node biopsy in breast cancer. *Annals of Oncology* **13**, 1531–1537 (2002).

14. Chow, E. K. *et al.* Nanodiamond therapeutic delivery agents mediate enhanced chemoresistant tumor treatment. *Science translational medicine* **3**, 73ra21 (2011).
15. Fu, C.-C. *et al.* Characterization and application of single fluorescent nanodiamonds as cellular biomarkers. *Proceedings of the National Academy of Sciences of the United States of America* **104**, 727–32 (2007).
16. Faklaris, O. *et al.* Detection of single photoluminescent diamond nanoparticles in cells and study of the internalization pathway. *Small (Weinheim an der Bergstrasse, Germany)* **4**, 2236–9 (2008).
17. Chang, Y.-R. *et al.* Mass production and dynamic imaging of fluorescent nanodiamonds. *Nature nanotechnology* **3**, 284–8 (2008).
18. Baranov, P. G. *et al.* Enormously high concentrations of fluorescent nitrogen-vacancy centers fabricated by sintering of detonation nanodiamonds. *Small (Weinheim an der Bergstrasse, Germany)* **7**, 1533–7 (2011).
19. Kok, P. & Lovett, B. W. Materials science: qubits in the pink. *Nature* **444**, 49 (2006).
20. Ladd, T. D. *et al.* Quantum computers. *Nature* **464**, 45–53 (2010).
21. Maze, J. R. *et al.* Nanoscale magnetic sensing with an individual electronic spin in diamond. *Nature* **455**, 644–7 (2008).
22. Balasubramanian, G. *et al.* Nanoscale imaging magnetometry with diamond spins under ambient conditions. *Nature* **455**, 648–51 (2008).
23. Shin, C. *et al.* Sub-optical resolution of single spins using magnetic resonance imaging at room temperature in diamond. *Journal of Luminescence* **130**, 1635–1645 (2010).
24. McGuinness, L. P. *et al.* Quantum measurement and orientation tracking of fluorescent nanodiamonds inside living cells. *Nature nanotechnology* **6**, 358–63 (2011).
25. Yang, N. & Cohen, A. E. Optical imaging through scattering media via magnetically modulated fluorescence. *Optics Express* **18**, 25461 (2010).
26. Goodwill, P. W. & Conolly, S. M. The X-space formulation of the magnetic particle imaging process: 1-D signal, resolution, bandwidth, SNR, SAR, and magnetostimulation. *IEEE transactions on medical imaging* **29**, 1851–9 (2010).

27. Das, B. B., Liu, F. & Alfano, R. R. Time-resolved fluorescence and photon migration studies in biomedical and model random media. *Reports on Progress in Physics* **60**, 227–292 (1997).

Supplementary Information is available in the online version of the paper.

ACKNOWLEDGEMENTS: A.H. acknowledges funding from a P. Michael Farmwald Fannie and John Hertz Foundation fellowship. This project was supported by the NSF Center for Scalable and Integrated NanoManufacturing (SINAM) and the DARPA-QuEST program. A.H. acknowledges discussion with M. Lustig, P. Goodwill, S. Conolly, and D. Hegyi. We thank H.-C. Chang for providing the nanodiamonds.

AUTHOR CONTRIBUTIONS: A.H. conceived the idea, designed the experiment, built the equipment, performed the experiment and wrote the paper. E.Y. provided funding and support and reviewed the manuscript.

AUTHOR INFORMATION: Alex Hegyi*, EECS Department, UC Berkeley. Competing interest statement: filed for a provisional patent related to this work. Prof. Eli Yablonovitch, EECS Department, UC Berkeley. *Corresponding author. Email: hegyi@eecs.berkeley.edu.

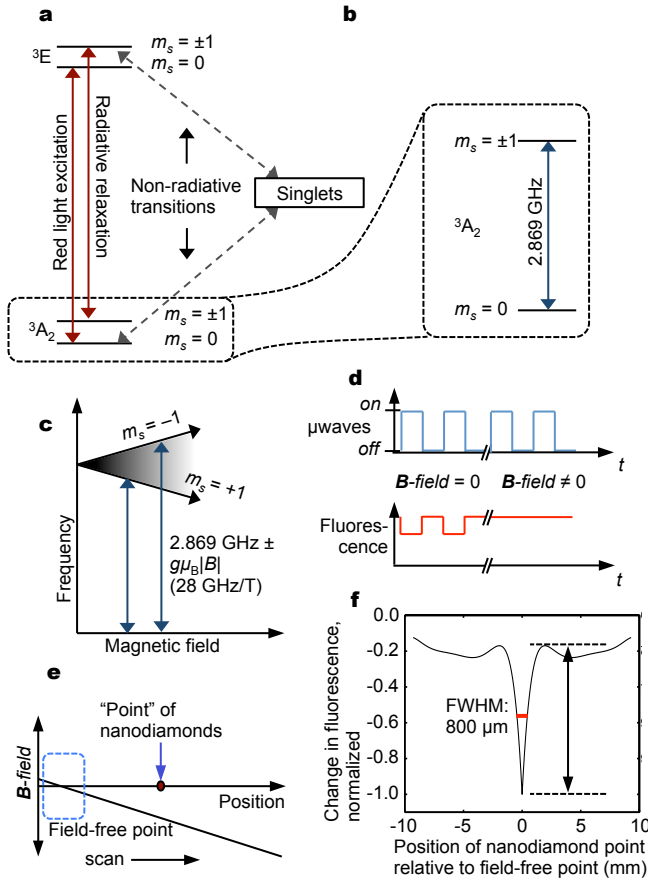


Figure 1 | NV optical transitions lead to optically-induced spin pumping and optically detectable spin state. **a**, Electronic level structure of the NV, depicting spin-conserving radiative transitions as well as nonradiative transitions, through singlet states, from $m_s = \pm 1$ to $m_s = 0$. Upon optical cycling the spin ends up in the $m_s = 0$ state, which fluoresces brighter than the $m_s = \pm 1$ states. **b**, The 2.869 GHz transition between $m_s = 0$ and $m_s = \pm 1$, in the absence of magnetic field (or strain). **c**, A magnetic field along the NV spin axis splits the spin transitions; in nanodiamond powder, transitions occur at all frequencies (indicated by the grayscale) in between the two extreme frequencies, because of the random orientations of the nanodiamonds relative to the field. **d**, Under optical excitation, chopping 2.869 GHz microwaves produces a synchronous modulation in fluorescence at the chopping frequency, but only in the absence of a magnetic field. **e**, **f**, Scanning a field-free point across a point of nanodiamonds (**e**) with microwaves on and tracking the fluorescence yields the imaging point-spread function (**f**). The height of the central peak, indicated by the two dashed lines with a FWHM of 800 μm , is 87% of the full height.

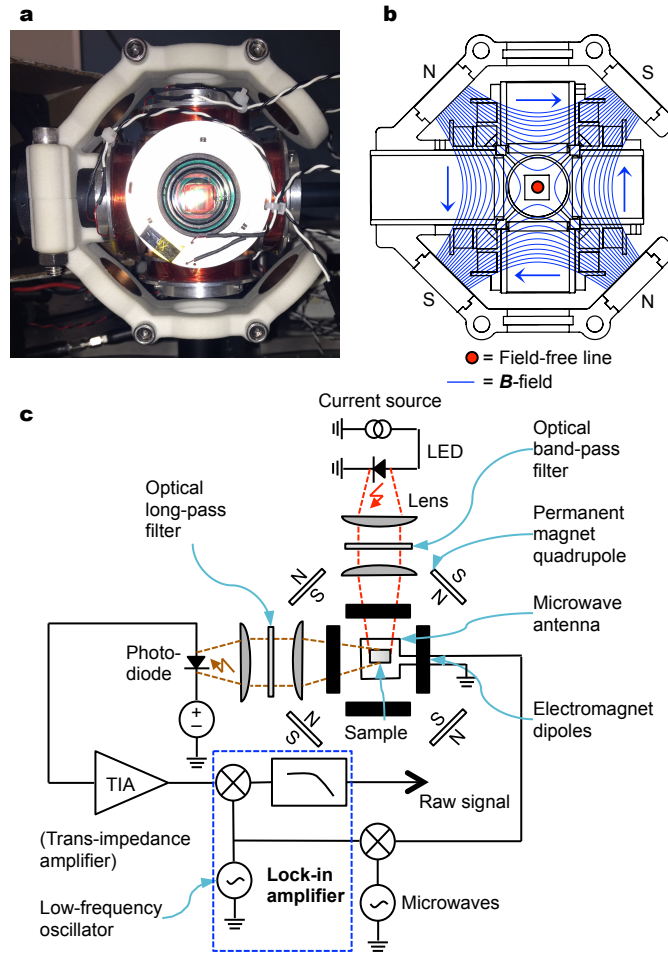


Figure 2 | Nanodiamond imaging apparatus. a, Photo of the apparatus. Permanent magnets are held by the white arms; electromagnet coils (copper wire) are visible as well. **b**, Cross-section of the imaging apparatus showing orientation of permanent magnets. The square in the middle is the 1 cm x 1 cm field of view. **c**, A schematic of the imaging system.

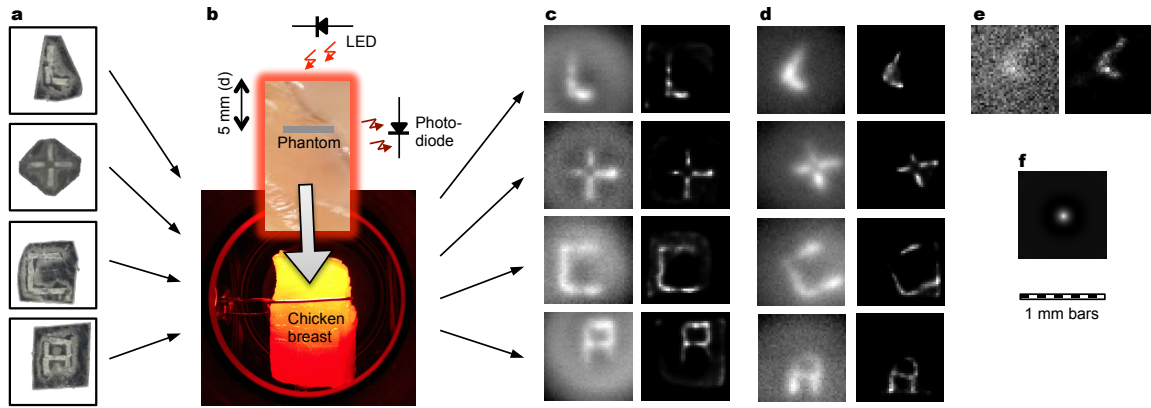


Figure 3 | A summary of the data. **a**, Nanodiamond phantoms made of double-sticky tape and nanodiamonds, shown at the same scale as the rest of the images. **b**, The grey stripe on the piece of chicken breast represents the edge of the phantom, which is placed inside the chicken breast, 5 mm back from the front surface, facing the LED. Fluorescence is collected off to the side. Also shown is the actual piece of chicken breast illuminated by the LED. **c**, The phantoms imaged outside of chicken breast, both before (left) and after (right) deconvolution by the point-spread function. **d**, Same as c but under 5 mm chicken breast. **e**, Image of the 'L' phantom under 12 mm chicken breast, before and after deconvolution. **f**, Point-spread function. All images are shown with a linear grayscale lookup table that spans the full range of the data in each image.

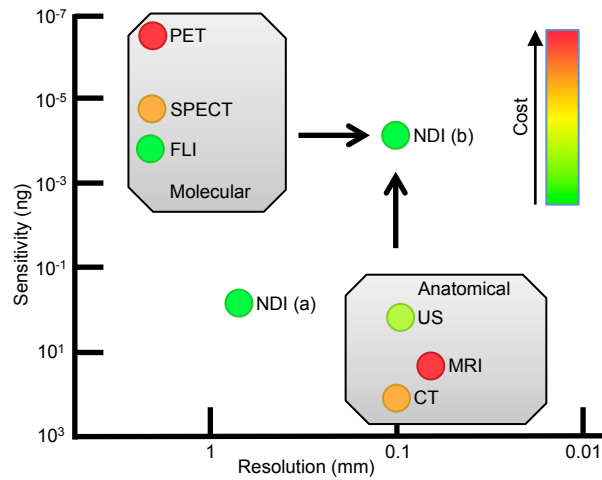


Figure 4 | Comparison of nanodiamond imaging to existing techniques. Both the current implementation of nanodiamond imaging (NDI (a)) and future implementation (NDI (b), with 0.03 % of potential sensitivity improvements, and reasonable increase in resolution) are compared to popular existing molecular and anatomical imaging techniques, in terms of mass sensitivity, resolution, and cost. FLI: fluorescence imaging; US: ultrasound.

Supplementary Information 1: Details of apparatus

Optical excitation from a heatsink-mounted red LED (Luminus CBT-120, HK flux bin, R4 wavelength bin—619 to 623 nm) driven at 18.0 A through a 10 mH inductor (Hammond 195J20), collimated with an aspheric condenser (Thorlabs ACL2520-A) and bandpass-filtered (Semrock FF01-615/45-25), was focused onto the sample with a lens (Thorlabs LA1422-A). All optics were placed in Thorlabs lens tubes, and black-flocked paper (Protostar FBR-01) covered all exposed surfaces of the lens tube interiors to minimize the propagation of scattered out-of-band light through the interference filters. Fluorescence emission was collected at a 90 degree angle to the excitation, through a first filter stage consisting of a condenser lens (Thorlabs ACL2520-B), a long-pass filter (Semrock LP02-664RS-25), and a second condenser lens (Thorlabs ACL2520-B) focused down onto an adjustable iris, then a second filter stage of the same lens/filter/lens combination, and finally focused onto a 10 mm x 10 mm Si photodiode (Hamamatsu S2387-1010R), reverse-biased at 15 V. A front-end preamplifier was built within the lens tube directly behind the photodiode, utilizing a low-noise JFET operational amplifier (Analog Devices ADA4627-1) in a standard transimpedance configuration. A feedback network of 10 M Ω in parallel with 10 pF was used. With this preamplifier, the detection system was shot-noise limited.

The output of the preamplifier was AC coupled to the input of a low-noise voltage preamplifier (Stanford Research Systems SR560), with the high-pass filter cutoff set at 100 Hz and the low-pass filter cutoff set at 1 KHz. Gain was set to 10^3 . The output of the SR560 was digitized at 250 KHz by a data acquisition (DAQ) card (National Instruments PCIe-6321).

Microwaves were generated by an analog signal generator (Agilent E8257D) set to 2.869 GHz at +24 dBm output power. The microwaves were chopped at 379 Hz by a PIN switch (Mini-Circuits ZASWA-2-50DR+) controlled by a digital output of the DAQ. Microwaves were transmitted to the sample via a ~12 mm x 12 mm square loop of 24 AWG solid copper wire, positioned around the perimeter of the sample.

A magnetic field-free line was generated by four 1"Ø x 3/8" neodymium magnets (K&J Magnetics SD06-OUT) as in Fig. 2. Electromagnet coils, used to raster the field-free line across the sample, were wound on spools machined to interlock with Thorlabs lens tube construction. The coils consisted of ~200 turns of 24 AWG magnet wire. Note that due to the 45° rotation of the permanent magnets relative to the electromagnets, the electromagnets in the horizontal direction move the field-free line vertically, and vice versa. A custom programmable bipolar power supply with a gain of 1 A/V was built to power the electromagnets, connected to the output of an analog output board (National Instruments PCI-6722).

The measurement software was written in LabVIEW. It generates an image by raster scanning the current in the electromagnets, thereby moving the field-free line across the field of view, to measure image intensity across a grid of points. At each point in the raster scan, the software executes the following sequence: it samples the output of the low-noise voltage preamplifier at 250 KHz, while chopping the microwaves at 379 Hz. Data is recorded for a specified time ($\tau_{\text{meas}} = 0.5$ s for all images shown in this letter) and

then passed through a series of digital filters: an elliptic 5th order band-pass with a 310 Hz lower cutoff and 450 Hz upper cutoff, an elliptic 5th order band-stop with a 55 Hz lower cutoff and 65 Hz upper cutoff, and an elliptic 5th order band-stop with a 115 Hz lower cutoff and a 125 Hz upper cutoff. The signal is then digitally mixed with cosine and sine waves with the same frequency as the microwave chopping frequency (379 Hz), to obtain the signal's X and Y (or in-phase and quadrature) components, respectively. Six copies of the resultant signals are concatenated and then filtered by a 4th order IIR Butterworth low-pass filter with a cutoff frequency of $1/(2\tau_{\text{meas}})$ Hz, pass-band ripple of 1 dB, and stop-band attenuation of 60 dB. The concatenation is to account for the rise-time of the filter, and care is taken to ensure that the phase of each signal to be concatenated is the same at its beginning and end. The X and Y components are combined into a polar representation of the signal (i.e., R and θ), and the last N samples of each signal are averaged ($N = \tau_{\text{meas}} * 250 \text{ KHz}$) to obtain the image intensity at a particular field-free line location. The process is repeated for each point in the image.

Supplementary Information 2: Sample preparation and imaging

NV-implanted (fluorescent) nanodiamonds (FNDs) were obtained from Prof. Huan-Cheng Chang of the Institute of Atomic and Molecular Sciences, Academia Sinica, Taipei, Taiwan. The details of FND production are explained elsewhere^{17,28}; briefly, synthetic type Ib diamond powder was irradiated with a 40 keV He⁺ beam, annealed in vacuum at 800 °C, oxidized in air at 450 °C, and cleaned with a concentrated sulfuric acid/nitric acid treatment, yielding a final nanodiamond diameter of 100 nm and an NV concentration of ~6 ppm. FNDs were washed with distilled, de-ionized water and provided to us as a 1 mg/ml suspension in water.

To make the nanodiamond phantoms, 2x2 mm squares of double-sticky tape were cut using a laser cutter. A 5 μl drop of the FND suspension was placed on each square of double-sticky tape and dried by placing it ~20 cm under a heat lamp. Two more additions of FND to each square of tape were made, to yield a $3.75 \mu\text{g mm}^{-2}$ areal density of FND on the tape. Each square was cut into 4 pieces of roughly 500 $\mu\text{m} \times 2 \text{ mm}$, and arranged into the various shapes shown in Fig. 3a: 'L', '+', 'C', and 'A'. The pieces of double-sticky tape were sealed between two pieces of Bio-Rad optical sealing tape.

Pieces of chicken breast were prepared by freezing chicken breast (Trader Joe's Organic) and cutting into 10 mm x 10 mm x 20 mm ingots. An incision was made 5 mm back from the front of each piece and a phantom was inserted into the incision (see Fig. 3b). For each phantom, image raw data were taken in a 40 x 40 grid over the 1 cm² field of view, with a 0.5 s measurement time at each pixel.

Supplementary Information 3: Processing of raw data: microwave feed-through subtraction, derivation of point-spread function, and subsequent deconvolution

Chopping of the microwaves produced a background component in the signal most likely due to the rectification of the chopped microwaves by the photodiode. Since this "microwave feed-through" signal occurred at the same frequency as the signal of interest, it showed up in the raw data as an additive background with a particular magnitude and

phase. The magnitude and phase of this background were determined by a measurement of the signal with the LED powered off.

Even though only the magnitude component of the signal was recorded when imaging the phantoms, a vector subtraction could still be performed to find the magnitude of the signal component that excluded the microwave feed-through. If x is the uncorrected image magnitude and b is the magnitude of the microwave feed-through, then the corrected image magnitude y is $y = \sqrt{|x^2 - b^2 \sin^2 \alpha|} - b \cos \alpha$ where α is the phase angle between the microwave feed-through and the hypothetical background-free signal (obtained by subtracting the microwave feed-through from a signal that included both magnitude and phase information). Note the absolute value around the radicand: in the absence of noise, the radicand would always be positive; however, for $x \approx b$, noise occasionally makes the radicand negative. Including the absolute value thus avoids unphysical complex image magnitudes, and does not appear to have an adverse effect on the images.

To derive the point-spread function (PSF), a 2 mm x 2 mm piece of double-sticky tape was coated with a $3.75 \mu\text{g mm}^{-2}$ areal density of nanodiamonds as described above in Supplementary Information 2. The piece was cut into four 500 μm wide x 2 mm long strips, and the strips were stacked on top of one another, to yield a “test object” of 15 μg nanodiamond arranged in a roughly 0.5 mm x 0.5 mm x 2 mm volume. The test object was placed lengthwise into the end of a glass pipette, and introduced into the imaging system such that the long axis was parallel to the field-free line. An image was taken by scanning 100 x 100 pixels across the 1 cm^2 field of view, with $\tau_{\text{meas}} = 1$ s at each pixel. The microwave feed-through, as described above, was subtracted from the image, and the resulting image was deconvolved with a 0.5 mm x 0.5 mm square (the on-axis profile of the test object) in an attempt to obtain the true PSF. The deconvolution was done in MATLAB, using 10 iterations of a Richardson-Lucy algorithm.

Next, the location of the peak value of the resulting data was found, and the data was mapped by bilinear interpolation onto a 2D polar coordinate grid with the origin at the location of the peak value, with grid spacing $\Delta r = 0.1$ mm and $\Delta \phi = 2\pi/300$ radians. For a given radial coordinate, the PSF was summed over the azimuthal coordinate to obtain the PSF as a function of the radial coordinate only (i.e., $\text{PSF}(r) = \sum_{\phi} \text{PSF}(r, \phi_i)$). Then, a 6th order polynomial, $\text{PolyFit}(x)$, was fit to $\text{PSF}(r)$. The final one-dimensional PSF, shown in Fig. 1f, is $\text{PolyFit}(|x|)$. To obtain a 2D PSF for deconvolution of the measured data, $\text{PolyFit}(r)$ is sampled on a 40 x 40 grid (same as the measured data) with $r^2 = x^2 + y^2$, and $x_i, y_i \in \{-5.00, -4.75, \dots, 4.75\}$, i.e., offset in the horizontal and vertical directions by half a pixel such that $r = 0$ at the center of one pixel, as shown in Fig. 3f.

For each image except the ‘L’ under 12 mm chicken, the microwave feed-through was subtracted, and then the image was deconvolved by the PSF shown in Fig. 3f. A Richardson-Lucy (RL) algorithm was used to do the deconvolution, as part of DeconvolutionLab²⁹, an add-on for the ImageJ software package. The stopping point for this iterative algorithm was arbitrarily set to 10,000 iterations. As illustrated in Fig. S1, stopping too soon does not allow the algorithm to fully remove the blur from the PSF’s

wide tails (see Fig. 1f), yet too many iterations produces a pixelated image due to the noise gain inherent in deconvolution.

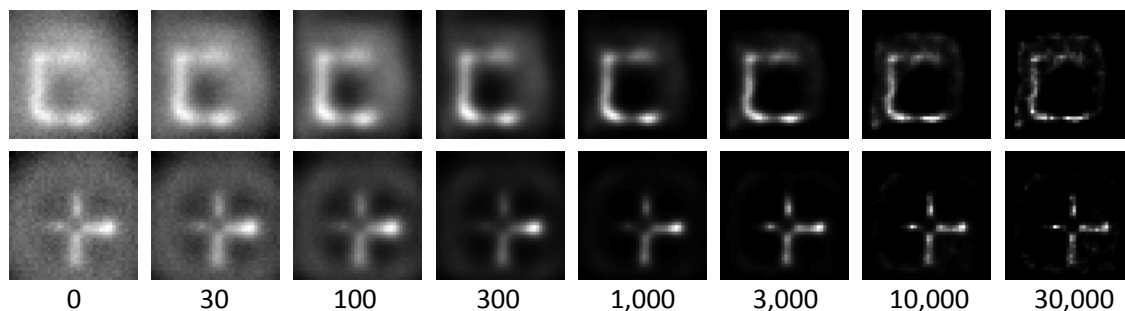


Figure S1: Richardson-Lucy deconvolution of images for ‘C’ and ‘+’ phantoms as a function of the number of iterations.

For the ‘L’ under 12 mm chicken, no microwave feed-through subtraction was done, as doing so appeared to prevent convergence of the RL algorithm (this may have to do with the low SNR of that particular image). Also, only 1,000 iterations of the RL algorithm were used, so the image would not have too much noise amplification. The 12 mm deep image is included only to demonstrate that it is possible to image that deeply.

Richardson-Lucy will converge to the maximum-likelihood solution for an image corrupted by noise with Poisson statistics (that is, where the noise variance follows the image intensity, as it normally does with the shot noise inherent in photon-based imaging). Our images are corrupted by noise with Gaussian statistics: the variance of the shot noise of the recorded photons is the same in each pixel, as it depends on the unmodulated fluorescence background, which is constant during the imaging process. Although the RL algorithm can be modified to converge to the maximum-likelihood solution assuming Gaussian statistics, the unmodified RL produced satisfactory results. In addition, to simplify the estimation of the nanodiamond distribution from the recorded image, a shift-invariant PSF was assumed (i.e., it was assumed that the imaging process represented convolution with a PSF) rather than a more general space-varying model. Because convolution doesn’t take into account position-dependent sensitivity, the estimated nanodiamond concentration at a given point will be off by a factor that depends on the sensitivity at that point. Hypothetically, the sensitivity function can be recorded in a calibration to correct for its effects after deconvolution, although in practical conditions, the sensitivity will depend on the distribution of tissue between the nanodiamonds and the imaging system.

Supplementary Information 4: Measurement and calculation of sensitivity

To measure the sensitivity of the current system, a piece of double-sticky tape 2 mm x 100 μ m, covered with 250 ng of nanodiamond, was prepared by cutting a \sim 100 μ m sliver off of a 2 x 2 mm piece of double-sticky tape, prepared according to Supplementary Information 2 (but using only a single 5 μ l drop of nanodiamond solution). This piece of double-sticky tape was placed lengthwise into the end of a glass pipette, which was placed parallel to the field-free line. An image was recorded with the same parameters

used to record the image of the PSF, as described in Supplementary Information 3. As before, the microwave feed-through component was subtracted from the resultant image. To estimate the noise, with the LED on and the microwaves off, the photodiode preamplifier's output was connected to a lock-in amplifier (Stanford Research Systems SR830) with a 100 ms time constant, selecting the “x-noise” measurement. The peak signal of the image was divided by the noise to get the SNR, which was $9.5 \text{ Hz}^{1/2}$. The sensitivity is thus $(250 \text{ ng})/(9.5 \text{ Hz}^{1/2}) = 26 \text{ ng Hz}^{-1/2}$ or $2.2 \text{ mM mm}^3 \text{ Hz}^{-1/2}$, expressed in terms of the concentration of carbon atoms in a mm^3 voxel.

There are many potential avenues for the improvement of the sensitivity of the nanodiamond imaging system, summarized in Table S1 below. Some of these relate to the nanodiamond material: it has been shown that sintering detonation nanodiamond may produce up to a 1% (10,000 ppm) concentration of NVs in the nanodiamonds¹⁸. Also, a bottom-up synthesis of NV-nanodiamond clusters, for example starting with nitrogen-functionalized diamondoids³⁰, may offer the potential to engineer out the strain in the nanodiamonds which causes inhomogeneous broadening. Doing so would create a sharper “line”, increasing the signal at the center of the PSF and decreasing the width of the PSF. It could also potentially yield a high NV concentration.

Other sensitivity enhancements would come from modifying the imaging approach from a continuous, quasi-static measurement scheme to one that is more dynamic. For example, switching to pulsed optical excitation is one way to increase the sensitivity: for the same optical energy in a measurement cycle, concentrating it in a duty factor $D < 1$ yields an SNR improvement of $1/D$ because the higher optical intensity generates a higher spin polarization, enabling a greater modulation depth in the NV fluorescence. By appropriately pulsing the microwaves, we can double the fluorescence modulation depth by fully inverting the spin population (for example by adiabatic fast passage³¹), rather than just equalizing the spin population between brighter and darker states, which is what happens with continuously-applied microwaves. (Also, pulsed microwaves would allow more rapid imaging because the fluorescence could be modulated as quickly as the spins could be inverted, whereas the current scheme relies on the spins being optically repumped each time the microwaves are turned off). Finally, applying time-gated fluorescence collection would enhance sensitivity because tissue autofluorescence occurs on a shorter timescale than fluorescence of NVs¹⁶, and time-gating the detectors could also prevent excitation light that scattered through the optical interference filters from registering. Decreasing these unmodulated background components by a factor α would result in a sensitivity increase of $\alpha^{1/2}$, as the shot noise only decreases with the square root of the background intensity.

Additional sensitivity enhancements are expected from enhancing the fluorescence collection efficiency (sensitivity scales as the square root of efficiency), as well as from incorporating a provision for cooling the organism so higher optical excitation intensities can be used. Note that at excitation intensities that might be used in practice, the spin polarization fraction is small, so sensitivity scales as the $3/2$ power of excitation intensity: a factor of 1 because of the increased fluorescence modulation caused by the increased spin polarization, and a factor of $1/2$ because of the increase in unmodulated background fluorescence.

Parameter to improve	Expected improvement	Sensitivity increase
Materials enhancements		
<i>Concentration of NVs in nanodiamond</i>	6 ppm → 10,000 ppm	1,666x
<i>Strain of nanodiamonds</i>	5 MHz → 1 MHz	5x
Taking advantage of dynamics		
<i>Duty factor of light pulsing</i>	100 % → 10 %	10x
<i>Fluorescence modulation depth</i> increase by full spin inversion	50 % → 100 %	2x
<i>Unmodulated background</i> decrease by time-gating fluorescence collection	100 % → 10 %	3.2x
General system optimization		
Improved <i>light collection efficiency</i>	100 % → 300 %	1.7x
Increased <i>optical excitation intensity</i> (by water-cooling the organism)	100 % → 1,000 %	32x
Product of expected sensitivity increases ≈ 29,000,000x		

Table S1: Factors expected to contribute to the increases in sensitivity of nanodiamond imaging. For each parameter to improve (in italics), two numbers are given in the second column: one indicating a relative or absolute value of the parameter in the current experiment, as well as a reasonable estimate of how much that parameter could be enhanced. Listed in the last column are the projected sensitivity increases due to each expected parameter improvement.

Supplementary Information 5: Creation of Figure 4

Four references were used in the compilation of Figure 4: Table 1 of Ref. [1], Table 2 of Ref. [32], Table 1 of Ref. [33] and Table 1 of Ref. [34]. For a given imaging modality, the sensitivity was calculated by taking the lowest and highest sensitivities quoted in all four references, and finding the geometric mean. Note that the sensitivities in Ref. [34] are described in terms of molar quantities, rather than concentration, of contrast agent. Using a reference volume of 1 cm³ appeared to produce sensitivities consistent with the other references. Only Refs. [33] and [34] were used for CT, and only Ref. [34] was used for US. Although other data were available for US in the other references, they referred specifically to microbubble contrast agents, which are highly sensitive with US (10⁻¹² M) but cannot escape the vasculature. Although we had no data to compare the sensitivity of US in Ref. [34] to, we assumed the 1 cm³ reference volume still held.

To compute the noise bandwidth for direct comparison of the sensitivity of nanodiamond imaging to the sensitivities listed in the references where no noise bandwidth was given, a measurement time of 100 s was assumed. This gave an equivalent noise bandwidth of 780 μHz for a 24 dB/octave filter such as in the SR830 lock-in amplifier. To go from

concentration of imaging agent to absolute quantity of imaging agent in moles, a voxel volume of 1 mm³ was assumed. Finally, to go from molar sensitivity to mass sensitivity, a representative molecular weight was chosen for each modality according to Table S2, below. Although up to a 29,000,000x sensitivity improvement has been identified for nanodiamond imaging, we only included a 10,000x improvement beyond the current sensitivity in the figure.

Modality	Imaging agent	Molecular weight (g/mol)
CT	iodine	127
MRI	magnevist	938
PET	18-FDG	181
SPECT	DOTA-tris(tBu)ester	573
FLI	IRDye 800CW	1165
US	*	154
NDI	Nanodiamond	12

Table S2: Molecular weights of prototypical contrast agents used to determine the mass sensitivity of each imaging modality (DOTA is a chelator). *For US, the geometric mean of the other molecular weights was used.

To find the resolution, for each modality, the geometric mean was taken across the lowest and highest values quoted in each reference. The color of each data point is a measure of the relative cost, as extrapolated from the information provided in the four references.

Supplementary References:

28. Fang, C.-Y. *et al.* The exocytosis of fluorescent nanodiamond and its use as a long-term cell tracker. *Small (Weinheim an der Bergstrasse, Germany)* **7**, 3363–70 (2011).
29. Vonesch, C., Cristofani, R. T. & Schmit, G. DeconvolutionLab. (2009). at <<http://bigwww.epfl.ch/algorithms/deconvolutionlab/>>
30. Dahl, J. E., Carlson, R. M., Liu, S. & Bokhari, W. Luminescent heterodiamondoids as biological labels. *US Patent App. 10/758,679* (2005).
31. Hardy, C. ., Edelstein, W. . & Vatis, D. Efficient adiabatic fast passage for NMR population inversion in the presence of radiofrequency field inhomogeneity and frequency offsets. *Journal of Magnetic Resonance (1969)* **66**, 470–482 (1986).
32. Levin, C. S. Primer on molecular imaging technology. *European journal of nuclear medicine and molecular imaging* **32 Suppl 2**, S325–45 (2005).
33. Sosnovik, D. & Weissleder, R. Magnetic resonance and fluorescence based molecular imaging technologies. *Imaging in Drug Discovery and Early Clinical Trials* **62**, 83–115 (2005).

34. Hahn, M. A., Singh, A. K., Sharma, P., Brown, S. C. & Moudgil, B. M. Nanoparticles as contrast agents for in-vivo bioimaging: current status and future perspectives. *Analytical and bioanalytical chemistry* **399**, 3–27 (2011).